ADVANCED ENERGY & SUSTAINABILITY RESEARCH
www.advenergysustres.com

Dispersion of InSb Nanoinclusions in Cu_3SbS_4 for Improved Stability and Thermoelectric Efficiency

Vaskuri C. S. Theja, Vaithinathan Karthikeyan, Dani S. Assi, Hongli Huang, Chan-Hung Shek, and Vellaisamy A. L. Roy**

Thermoelectric-based waste heat recovery requires efficient materials to replace conventional non-eco-friendly Te- and Pb-based commercial devices. Ternary copper chalcogenide-based famatinite (Cu_3SbS_4) compound is one of the practical substitutes for traditional thermoelectric materials. However, the pristine Cu_3SbS_4 inherits poor structural complexion, large thermal conductivity, and low power conversion efficiency. To develop high-efficiency Cu_3SbS_4, InSb nanoinclusions are incorporated via high-energy ball milling followed by the hot-press densification method. Incorporating InSb nanoinclusions to lower thermal conductivity via phonon scattering while increasing the thermopower via a carrier energy filtering process. The thermoelectric performance (ZT) of ≈0.4 at 623 K is obtained in Cu_3SbS_4-3 mol% InSb nanocomposite, which is ≈140% higher than pure Cu_3SbS_4. Both mechanical and thermal stability are improved by grain boundary hardening and dispersion strengthening. Thus, a facile nanostructured Cu_3SbS_4 with added InSb nanoinclusions is delivered as a highly efficient, eco-friendly, structurally-, thermally-, and mechanically-stable material for next-generation thermoelectric generators.

1. Introduction

Over the past few years, extensive research on thermoelectric materials has intensified due to their potent capacity to effectively convert heat into electrical energy. The advantages of solid-state, emission-free, and operation capacity over a wide temperature range make them important technology for waste heat recovery.[1] Thermoelectric conversion efficiencies are quantified by the relation, $ZT = \alpha^2\sigma T/\kappa$, where κ and σ represent thermal and electrical conductivities, α represents the thermopower or Seebeck coefficient, and T represents applicable temperature, respectively. The strong negative interrelation between the thermoelectric parameters (α, σ, and κ) complicates the challenge of improving the thermoelectric conversion efficiency in materials.[2] The phonon and electronic components of thermal conductivity are combined to make up the total thermal conductivity. The Wiedemann–Franz law relates the electrical conductivity and electronic components of thermal conductivity. One of the easy steps to improve thermoelectric performance is reducing the phonon component of thermal conductivity without interfering with electrical transport.[3] For this case, various strategies to reduce the phonon component of thermal conductivity are established, such as nanocompositing,[4–6] nanostructuring,[7,8] adding rattlers,[9] doping or alloying,[10–12] and defect engineering,[13–15] etc. Advantageously, the nanostructuring technique does not require extrinsic elemental additions and can be controlled by sintering.

According to statistics, 80% of waste heat from industries is released at temperatures between 373 and 573 K.[16] Though commercially available Te and Pb-based thermoelectric devices suit this intermediate temperature regime, they are toxic and pollute the environment. Generally, high conversion efficiency, good mechanical & thermal stability, low cost, and low toxicity material characteristics are essential for the large-scale production and commercialization of thermoelectric generators.[17] Satisfying this requirement, Cu-S-based chalcogenide compounds are considered promising *p*-type materials for thermoelectric applications.[17–19] Cu_3SbS_4 is one of the best alternative p-type thermoelectric compounds for intermediate-temperature applications.[20,21] Below their melting point, Cu_3SbS_4 is highly stable with a tetragonal crystal structure derived from its asymmetric zinc blend structure and does not show any secondary phase formations.[18] However, despite Cu_3SbS_4 good electrical characteristics, the issue of quite high thermal conductivity due to the uncomplicated lattice structure

V. C. S. Theja, C.-H. Shek
Department of Materials Science and Engineering
City University of Hong Kong
Kowloon Tong, Hong Kong

V. Karthikeyan, D. S. Assi, H. Huang
James Watt School of Engineering
University of Glasgow
Glasgow G12 8QQ, UK
E-mail: vaithinathan.karthikeyan@glasgow.ac.uk

V. A. L. Roy
School of Science and Technology
Hong Kong Metropolitan University
Ho Man Tin, Hong Kong
E-mail: vroy@hkmu.edu.hk

The ORCID identification number(s) for the author(s) of this article can be found under https://doi.org/10.1002/aesr.202300125.

DOI: 10.1002/aesr.202300125

and the absence of lone pairs of electrons impedes its thermoelectric efficiency.[17] The techniques such as nanostructuring by forming nanocomposite structures have been adopted to enhance their conversion efficiency.[22]

Nanostructuring in a thermoelectric material is achieved by the facile incorporation of secondary nanoinclusions in the matrix material. Nanoinclusions contribute to the reduction of thermal conductivity by utilizing interfacial boundary-based phonon scattering.[4,5,20,23] Given the similarity in sizes of the nanoinclusions with the phonon mean free path (MFP of phonons is greater than electrons), these interfacial boundaries effectively scatter phonons more than electrons.[24] Indium antimonide (InSb) intermetallic as a nanoinclusions can improve the thermoelectric efficiency of materials and enhance the material's ZT simultaneously.[25–33] Semiconducting InSb nanoinclusions are added in both ex situ and in situ manner. Ex situ processing route has advantages in terms of homogeneous distribution, eliminating unwanted secondary phase formations, and controlled particle size in maximizing the interfacial boundary region.[25,28,30] Huang et al.[26] demonstrated that 3 mol% InSb nanoinclusions in the $Cu_{12}Sb_4S_{13}$ matrix enhanced the thermopower via carrier energy filtering and degraded thermal conductivity via phonon scattering for maximized thermoelectric performance. Ghosh et al.[27] showed that ex-situ InSb nanoinclusions reduced the $CoSb_4$ matrix conductivity while improving the thermopower and reducing the thermal conductivity for overall improvement in thermoelectric performance.

On the other hand, solid-state mechanical alloying is advantageous over wet chemical synthesis in producing nanocrystalline powders in terms of product purity, synthesis simplicity, and processing speed.[22,34] In this work, ex situ InSb nanoinclusions were added to improve the thermoelectric performance of mechanically alloyed Cu_3SbS_4, employing interfacial boundary-assisted phonon scattering and energy filtering mechanisms. The nanocomposite Cu_3SbS_4-3 mol% InSb structure resulted in improved thermopower and reduced thermal conductivity. Additionally, InSb nanocomposite helps to improve the structural, thermal, and mechanical stabilities of the Cu_3SbS_4 structure. Through the microstructure and processing design, we achieve higher thermoelectric efficiency and improved thermal and mechanical stability using Cu_3SbS_4 thermoelectric material.

2. Results and Discussion

Table 1 shows the physical and structural parameters of the Cu_3SbS_4 samples we produced in this study. The measured densification in all the Cu_3SbS_4 samples exceeded 90%. The densification was lowered by adding InSb nanoinclusions due to the generation of back stress at the interfaces during sintering in the composites.[35]

Table 1. Crystalline size, density, densification, and porosity of the Cu_3SbS_4 samples.

Nanoinclusion [mol%]	Crystalline size [nm]		Calculated density [g cm^{-3}]	Compaction [%]	Effective mass (m_d^*)
	XRD	SEM			
0	78.57	75.43	4.31	94.31	1.19
1	72.26	65.98	4.26	93.42	1.97
3	69.08	58.51	4.27	93.64	2.82

The complete mechanical alloying route of the nanostructured Cu_3SbS_4 synthesis process is schematically illustrated in **Figure 1**a. The Cu_3SbS_4 crystal structure (tetragonal structure with $I\bar{4}2m$ space group) is shown in Figure 1b. X-ray diffraction (XRD) patterned peaks match those of the famatinite (Cu_3SbS_4, JCPDS: 35-0581) and the peak corresponding to the InSb (InSb, JCPDS: 06-0208) phase observed, as shown in Figure 1c. As noted in Table 1, the average size of grains is calculated from the XRD data using the Scherrer equation (Equation (1)) and from field emission scanning electron microscope fractured surface morphology (as shown in Figure S1, Supporting Information) using the ImageJ software. As mentioned in Table 1, the average grain size decreases with the increase in the concentration of InSb nanoinclusions. Adding harder nanoinclusions pins the grain boundaries and hinders grain growth during sintering.[36] However, the added InSb amount is too small, and most of the standard XRD Cu_3SbS_4 and InSb peak positions are matching; we carried out the Raman analysis to confirm the presence of the InSb phase. Raman spectra shown in Figure 1d revealed that the Cu_3SbS_4-related peaks displayed vibration modes at Raman shifts of 247, 273, 317, 344, 358, and 634 cm^{-1}. As shown in Figure 1d, Raman spectra also revealed the InSb peak at 186 cm^{-1} in composite samples that correspond to the longitudinal–optical (LO) phonon mode, which confirms the formation of the InSb phase.[37] As shown in Figure 1e, the backscattered electron scanning electron microscope (BSE–SEM) image indicates that the InSb nanoinclusions are distributed homogeneously in the Cu_3SbS_4 nanocomposite. The elemental mapping shown in Figure 1f exposes the elements that are distributed uniformly in the matrix and nanophase. The energy dispersive x-ray spectroscopy (EDX) compositional breakdown in Figure 1g revealed the presence of Cu, Sb, S, and In without oxygen in the Cu_3SbS_4 composite. From the XRD and EDX analyses, the absence of oxides or secondary phase peaks indicates the high phase purity of the synthesized Cu_3SbS_4 nanocomposite pellets.

$$D = \frac{0.9\lambda}{\beta \cos\theta} \tag{1}$$

where β denotes full width at half maxima, θ is the diffraction angle, λ is the wavelength of the XRD source, and D is the grain size.

From **Figure 2**a, according to measurements of the Hall effect, as the concentration of InSb nanoinclusions increased, carrier concentration ($\times 10^{20}$ cm^{-3}) increased, and carrier mobility decreased. The temperature-dependent Hall effect measurements of carrier concentration and carrier mobility are shown in Figure S2, Supporting Information. InSb is a nearly metallic phase with a narrow bandgap of 0.17 eV and possesses a very low electrical resistance of ≈18 μΩm at 300 K.[28] Therefore, the enhanced carrier concentration is significantly caused by the additional InSb semiconducting nanoinclusions. The mobility reduction observed is associated with the domination of carrier scattering in the high-density nanograin/interfacial structures.[34] According to Figure 2b and S2a, Supporting Information, it is

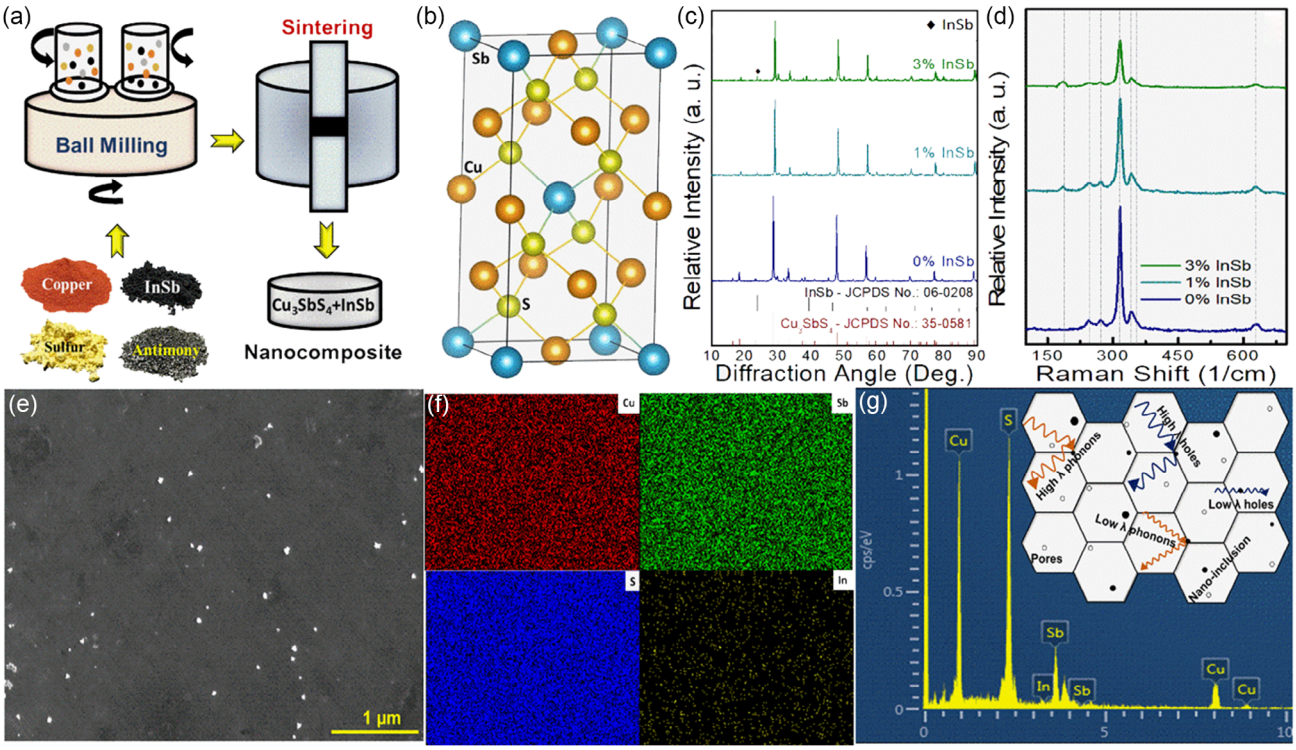

Figure 1. a) Synthesis route, b) crystal structure, c) XRD, d) Raman spectra, e) BSE–SEM micrograph of Cu_3SbS_4–3% InSb composite, f) elemental mapping, g) EDX with inset showing carrier scattering and filtering mechanisms in nanostructured Cu_3SbS_4.

observed that electrical conductivity increased with increasing temperatures due to the excitation of secondary carriers and the generation of electron–hole pairs with increasing temperatures in all the Cu_3SbS_4 samples. All Cu_3SbS_4 samples show increased electrical conductivity with the temperature that displays nondegenerate semiconducting behavior. According to Figure 2b, as the amount of InSb nanophase increased, the electrical conductivity decreased as a result of the predominance of reduced mobility through carrier scattering.[27] The Fermi level is theoretically determined by data from experiments using Equation (2) and (3).

$$S = \frac{k_B}{e}\left[\frac{2F_1(\eta)}{F_0(\eta)} - \eta\right] \tag{2}$$

$$E_f = \eta k_B T \tag{3}$$

where η is the reduced Fermi level, m_0 is the mass of the electron, k_B denotes Boltzmann's constant, T is applicable temperature, h is Planck's constant, and Fermi integral functions for η are $F_0(\eta)$, and $F_1(\eta)$. In all Cu_3SbS_4 samples, the Fermi level (E_f) increases with temperature as well as decreases due to an increase in the amount of InSb nanoinclusions, as shown in Figure 2c.

All synthesized Cu_3SbS_4 samples exhibit positive thermopower values, as illustrated in Figure 2d, which means p-type semiconducting behavior, thus indicating holes as major carriers. In all Cu_3SbS_4 samples, with increasing temperature, the thermopower values slightly increase. The thermopower also increases with the rising concentration of InSb nanoinclusions. Based on the bandgap difference and band alignment connecting the matrix and secondary phase, InSb nanoinclusions create interfacial boundaries that filter the carriers based on their relative energies. Gayner et al.[38] explained that the thermopower improved due to filtering energy-dependent charge carriers, which adds up to the enhanced normalized thermopower distribution. In Cu_3SbS_4 composites, nanocomposite structure results in carrier filtering or low-energy (energy-dependent) charge carrier scattering, as shown in the inset of Figure 1g. Mott's formula (Equation (4)) is used to theoretically compute the effective mass from the experimental data using the single-parabolic (SPB) model.

$$m_d^* = \frac{h^2}{2k_B T m_0}\left(\frac{p}{4\pi F_{1/2}(\eta)}\right)^{2/3} \tag{4}$$

where $F_{1/2}(\eta)$ denotes the Fermi integral function.

As noted in Table 1, the density of states' associated effective mass (m_d^*)increased with increasing the concentration of InSb nanoinclusions. Carrier mobility has an inverse relationship with (m_d^*), which is $m_d^{*5/2} \propto 2/\mu$, which agrees well with increasing the concentration of InSb nanoinclusions' increased effective mass. The SPB is supported by the Pisarenko relationship between the empirically determined thermopower and carrier concentration, which also explains the carrier energy filtering in nanocomposite structures, as illustrated in Figure 2e. Figure 2f shows that the temperature-dependent power factor increases with temperature in all the Cu_3SbS_4 samples. According to Figure 2f, the

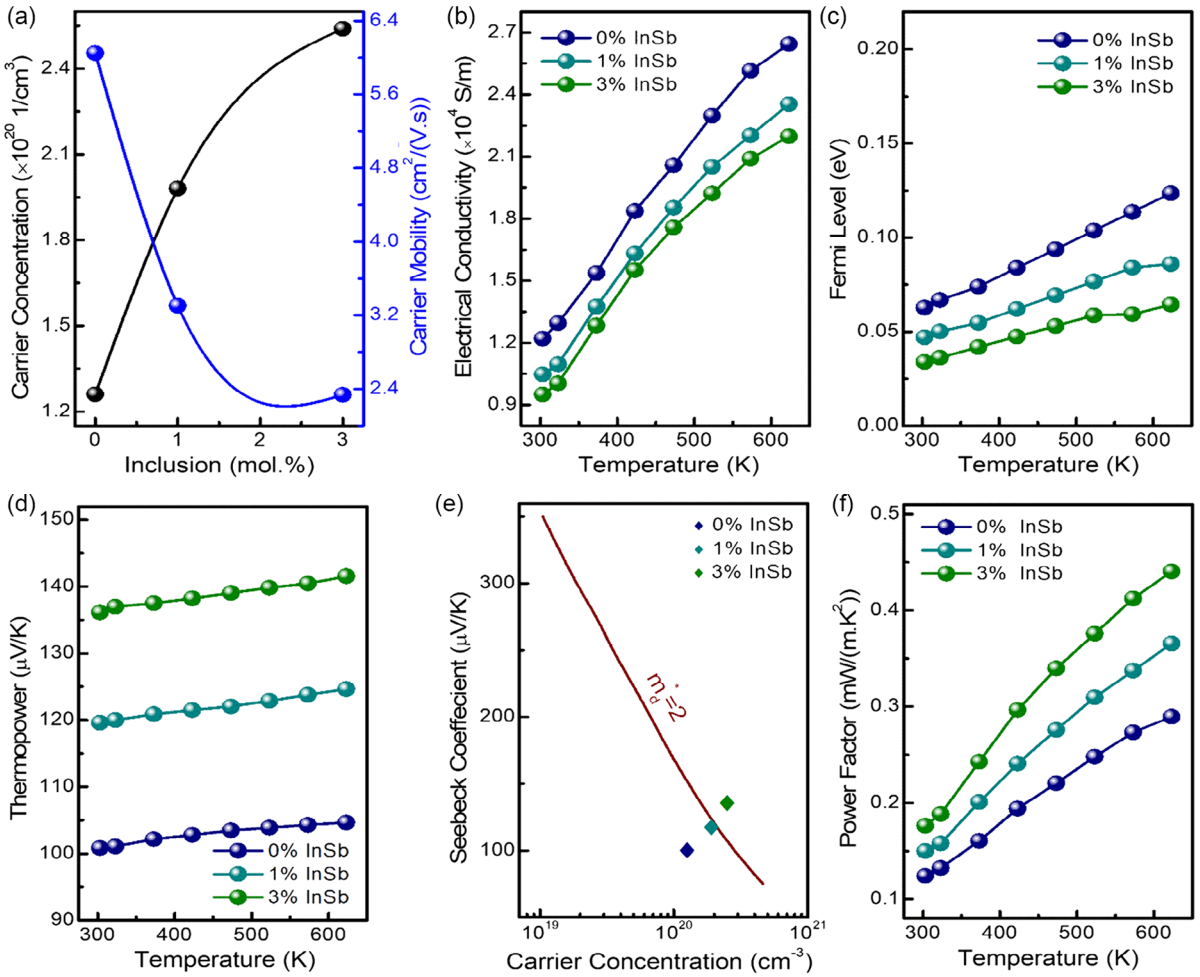

Figure 2. a) Carrier concentration and mobility, b) electrical conductivity, c) Fermi level, d) thermopower, e) Piserenko relation, and f) power factor of synthesized $Cu_3SbS_4 + x\%$ InSb ($x = 0$, 1, and 3) nanoinclusion samples.

thermopower enhancement by interfacial boundary filtering outweighs the reduction in electrical conductivity by boundary scattering; hence, the power factor increased as the concentration of InSb nanoinclusions increased.

According to **Figure 3**a, the total thermal conductivity is reduced with increasing temperature in all the Cu_3SbS_4 samples. Fine and high-density interfacial boundaries mainly scatter in the medium-to-long-wavelength phonons.[20] As per Figure 3a, Cu_3SbS_4 with 3% InSb nanoinclusions shows the smallest possible thermal conductivity of 0.73 W m^{-1} K^{-1}; it is ≈40% inferior to that of the pristine Cu_3SbS_4. The interfacial boundary-assisted phonon scattering generated in the Cu_3SbS_4 nanocomposite resulted in reduced thermal conductivity. As shown in the inset of Figure 1g and S1a–c, Supporting Information, mechanical alloying resulting in high densities of nanograin boundaries, embedded InSb nanoinclusions, and nanopores together contribute to the nanocomposite structures' reduced thermal conductivity. Kim et al.[39] explained the way to determine the Lorenz number using the equation $L = 1.5 + \exp(-|\alpha|/116)$ from the measured thermopower, where α is shown in μV K^{-1}; the derived values are shown in Figure 3b. As shown in Figure 3c, The Wiedemann–Franz law, $\kappa_{electronic} = L\sigma T$, is used to compute the thermal conductivity from electronic component ($\kappa_{electronic}$), where L denotes the Lorenz number, T denotes the applicable temperature, and σ represents the electrical conductivity. The electronic component of thermal conductivity exhibits the same electrical conductivity trend as minority carriers' excitation and increased electrical conductivity with temperature. According to Figure 3d, the thermal conductivity of phonon component (κ_{phonon}) is calculated using the equation: $\kappa_{total} = \kappa_{electronic} + \kappa_{phonon}$. From Figure 3e, κ_{phonon} contributes higher than $\kappa_{electronic}$ toward total κ due to the relatively lower electrical conductivity of Cu_3SbS_4 compared to traditional TE materials. As shown in Figure 3f, we showed κ_{phonon} versus 1000/T to illustrate the fundamental process underlying the phonon thermal conductivity in all the Cu_3SbS_4 samples. The negative slope of the solid linear connection with the increasing temperature between κ_{phonon} and 1000/T suggests the supremacy of the Umklapp phonon–phonon scattering process at higher temperatures in all Cu_3SbS_4 samples.[19,40] The thermoelectric performance (ZT) of InSb nanoinclusions added to Cu_3SbS_4 nanocomposite samples is shown in **Figure 4**a.

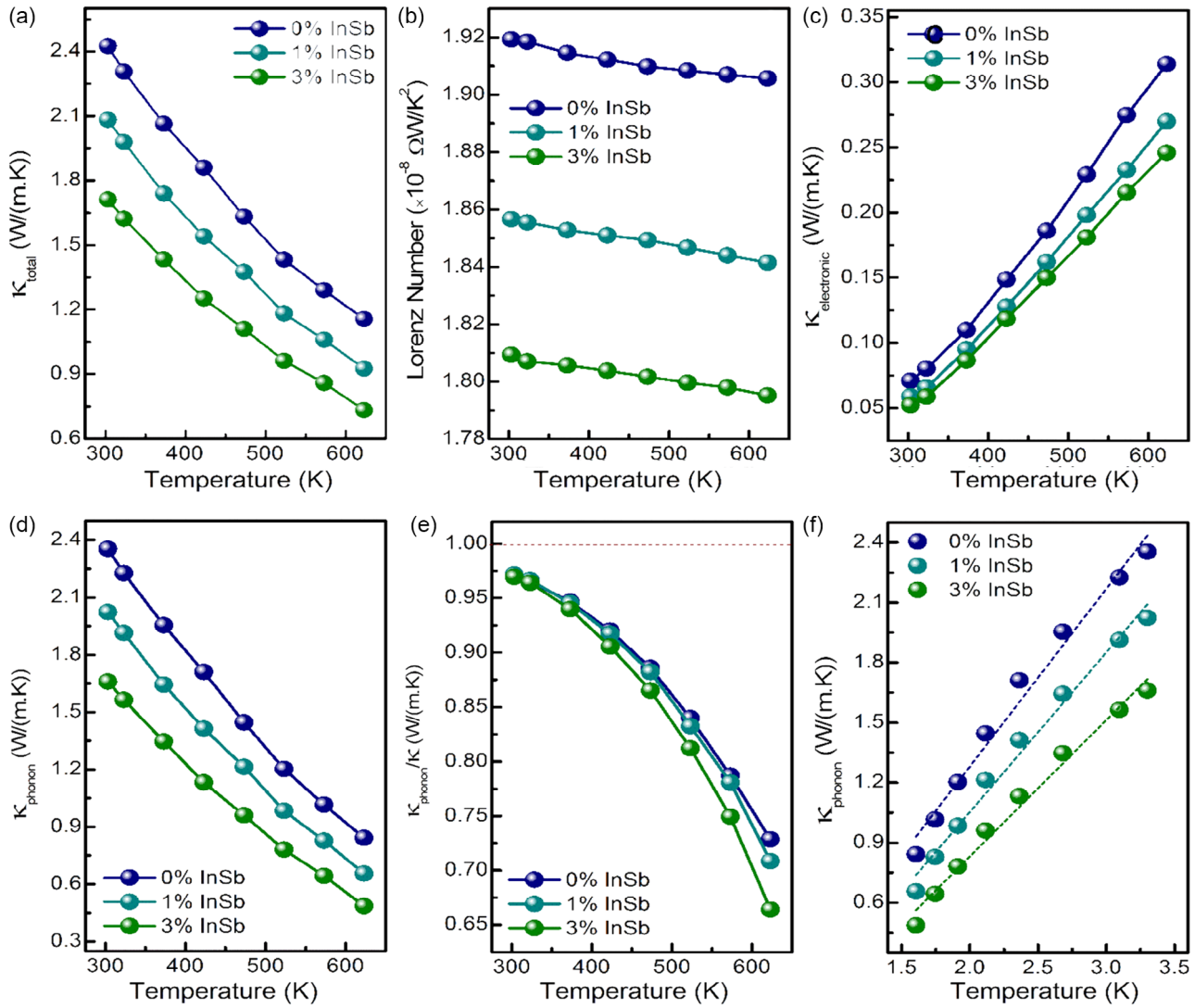

Figure 3. a) Total thermal conductivity, b) Lorenz number, c) electronic thermal conductivity, d) phonon thermal conductivity, e) phonon contribution on total thermal conductivity, and f) κ_{Phonon} versus 1000/T of $Cu_3SbS_4 + x$% InSb ($x = 0$, 1, and 3) nanoinclusion samples.

We demonstrated a maximum thermoelectric performance (ZT) of ≈0.4 in the 3 mol% InSb nanoinclusions added Cu_3SbS_4, which is ≈140% higher than pristine Cu_3SbS_4. The achieved ZT in the pristine Cu_3SbS_4 is higher than those reported in previous literature, as shown in Figure 4b. Using the determined ZT, we calculated the thermoelectric efficiency with Equation (5).

$$\eta = \frac{T_h - T_c}{T_h}\left[\frac{\sqrt{1+ZT}-1}{\sqrt{1+ZT}+(T_c/T_h)}\right] \tag{5}$$

As shown in Figure 4c, we achieved maximum thermoelectric efficiency of ≈5% in the Cu_3SbS_4–3 mol% InSb nanocomposite at 623 K.

According to Figure 4d, the differential scanning calorimetry (DSC) analysis revealed strong phase stability until the TE applicable temperature in all the Cu_3SbS_4 samples. From the DSC curves, it is evident that there are no exothermic peaks or thermal decomposition-related phase changes in all the Cu_3SbS_4 samples. Vickers microhardness, shown in Figure 4e, indicated that hardness improved sequentially (from 1.7 GPa in pristine Cu_3SbS_4 to 2.9 GPa in Cu_3SbS_4–3 mol% InSb sample) with increasing concentration of InSb nanoinclusions in Cu_3SbS_4 due to the dispersion strengthening and grain boundary hardening mechanisms.[41] The schematic illustrations of the improved mechanical stability-assisted mechanisms in the composite materials are shown in the Figure S4, Supporting Information. As shown in Figure 4f, thermogravimetric analysis (TGA) plots revealed the thermal stability (change in weight of greater than 98%) of both pristine and nanocomposite Cu_3SbS_4. As shown in Figure 4f, increasing the amount of InSb nanoinclusions in Cu_3SbS_4 composites improved thermal stability. To reassure the thermal stability, thermoelectric parameters have been measured repeatedly in three cycles and corresponding data (with error bars) shown in supporting information

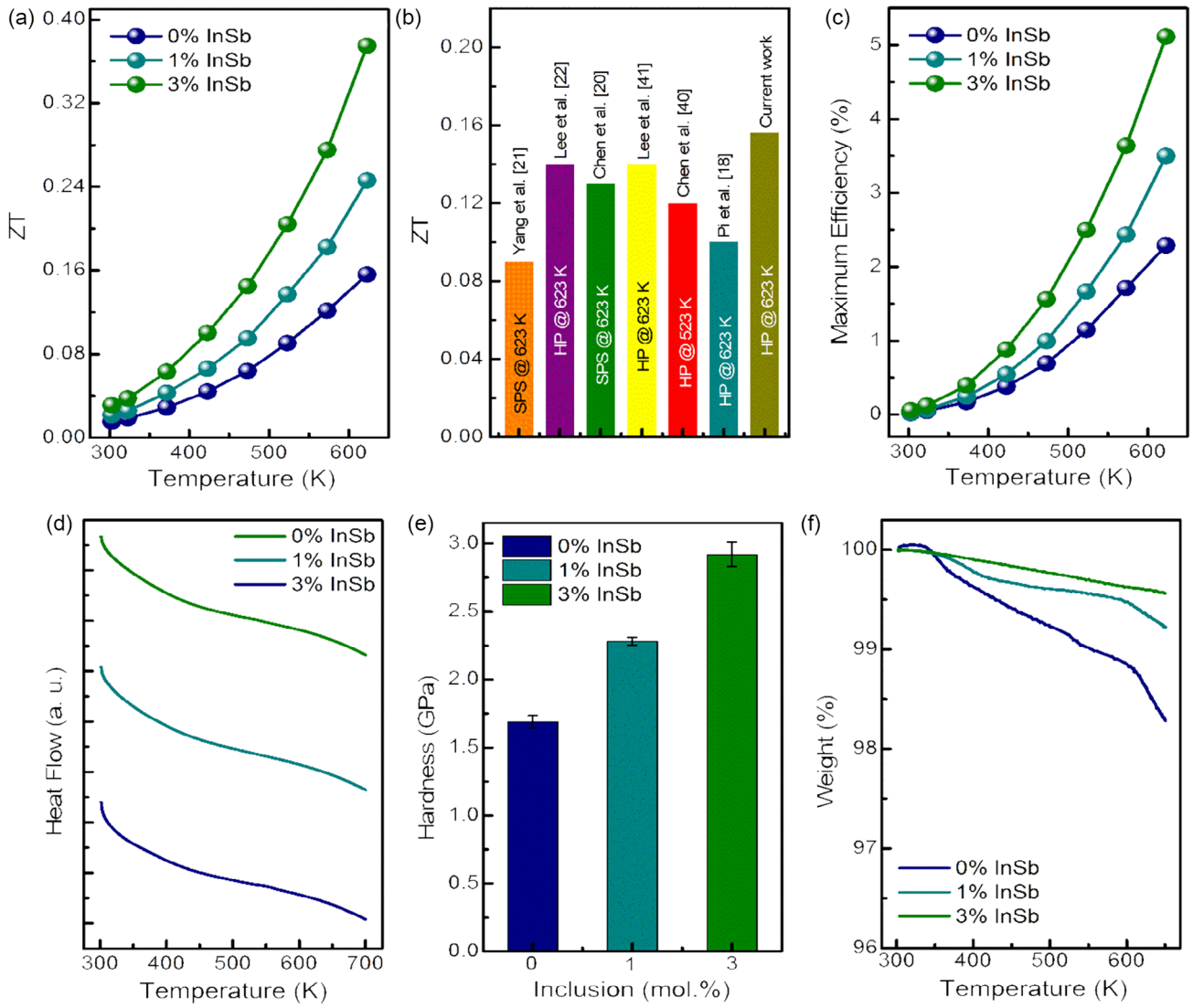

Figure 4. a) Figure of merit, b) comparison of ZT of various reported pristine Cu_3SbS_4,[5,18,20–22,42,43] c) obtained maximum efficiency, d) DSC phase stability, e) room-temperature Vickers hardness, and f) TGA thermal stability of $Cu_3SbS_4 + x$% InSb ($x = 0$, 1, and 3) nanoinclusion samples.

as Figure S3, Supporting Information. Therefore, synthesis of Cu_3SbS_4 by combining facile mechanical alloying with the incorporation of InSb nanoinclusions produces a nanostructured (fine grain boundaries plus interfaces) material with high thermoelectric performance, strong phase stability, and improved mechanical and thermal stability for next-generation intermediate-temperature applications.

3. Conclusion

In summary, InSb nanoinclusions incorporated Cu_3SbS_4 nanocomposite are synthesized through facile mechanical alloying followed by hot-press densification. By incorporating ex situ InSb nanoinclusions into Cu_3SbS_4, nanograin and interfacial barriers are created, which filtered low-energy charge carriers to increase the thermopower and minimize phonon thermal conductivity. As a result, the Cu_3SbS_4–3 mol% InSb nanocomposites show a maximum ZT of ≈0.4, which is ≈140% higher than pristine Cu_3SbS_4. Improved phase, thermal and mechanical stabilities are demonstrated with increasing InSb concentration due to dispersion strengthening and grain boundary hardening. From these observations, we believe that incorporating InSb nanoinclusions effectively generates a nanocomposite structure to improve the thermoelectric performance of Cu_3SbS_4.

4. Experimental Section

Stoichiometric high-purity powders of copper (company: Kurt. J. Lesker, purity: 99%), antimony (company: Kurt. J. Lesker, purity: 99.999%), sulfur (company: Sigma Aldrich, purity: 99.98%), and indium antimonide (company: Sigma Aldrich, purity: 99.99%) were weighed. The weighed powders were mixed and ground homogeneously using a pestle and mortar. In a high-energy planetary ball-milling machine, mechanical alloying was performed using ZrO_2 balls at 300 rpm for 24 h in a toluene medium with a ball-to-powder weight ratio of 20. Then the powders were compacted by hot pressing sintering in a cylindrical high-density graphite mold with a die

of 15 mm diameter at 350 °C under uniaxial pressure of 120 MPa for 10 min. Hot pressing was done in a hydraulic laboratory press (Model: 944 955, Dake Corp., USA). The processed samples' relative densities were then calculated using the conventional Archimedes method. The powder XRD method was used in a Bruker D2 Phaser with a Lynxeye detector to perform phase analysis using Cu Kα radiation of wavelength 1.54 Å. In order to comprehend the phase formations using vibrational intensities associated with chemical bonding, the WITec RAMAN alpha 300R system was used to record the Raman spectra at an excitation cobalt DPL laser wavelength of 532 nm. The JEOL JSM-IT500 SEM in MSE mode, elemental mapping, and EDX were employed for high-magnification fractography.

The electrical conductivity (σ) and thermopower (α) were measured using a typical four-probe direct current apparatus, that is, the SBA 458 Nemesis (Netzsch), in an argon environment. The Lakeshore Hall measuring system was used to evaluate the charge carrier transport (carrier mobility and concentration) in the magnetic field of −2–+2 T. Using measured carrier concentration and the thermopower, the density of the states associated effective mass (m_d^*)and Fermi level (E_f) were predicted. Using the laser flash method, thermal diffusivity measurements are carried out on disk samples with a diameter of 12.7 mm and thickness of 3 mm in the Netzsch LFA 467 equipment. The standard equation of thermal conductivity, $\kappa = \rho\alpha C_p$, was used in Netzsch-assisted software to automatically calculate thermal conductivity, where C_p stands for specific heat capacity, α stands for thermal diffusivity, and ρ is the sample's calculated density. The acquired thermopower, thermal, and electrical conductivity data were then used to calculate the power factor ($\alpha^2\sigma$) and the thermoelectric performance (ZT). Micro-Vickers hardness machine was used with a load of 5 kgf and a dwell duration of 10 s on test samples that were meticulously polished. The PerkinElmer STA6000 Simultaneous Thermal Analyzer performed TGA and DSC measurements to understand the phase and thermal stability.

Supporting Information

Supporting Information is available from the Wiley Online Library or from the author.

Acknowledgements

The authors acknowledge the support from the Research Grants Council of Hong Kong SAR under the Theme-based Research Scheme (T42-103/16-N).

Conflict of Interest

The authors declare no conflict of interest.

Data Availability Statement

The data that support the findings of this study are available from the corresponding author upon reasonable request.

Keywords

Cu_3SbS_4, InSb, nanoinclusion, thermoelectric

Received: July 3, 2023
Revised: August 21, 2023
Published online: September 8, 2023

[1] L. Han, S. H. Spangsdorf, N. V. Nong, L. T. Hung, Y. B. Zhang, H. N. Pham, Y. Z. Chen, A. Roch, L. Stepien, N. Pryds, *RSC Adv.* **2016**, *6*, 59565.
[2] B. Srinivasan, B. Fontaine, F. Gucci, V. Dorcet, T. G. Saunders, M. Yu, F. Cheviré, C. Boussard-Pledel, J. F. Halet, R. Gautier, M. J. Reece, B. Bureau, *Inorg. Chem.* **2018**, *57*, 12976.
[3] P. Roy, V. Pal, T. Maiti, *Ceram. Int.* **2017**, *43*, 12809.
[4] V. Karthikeyan, V. C. S. Theja, M. M. De Souza, V. A. L. Roy, *Phys. Status Solidi RRL* **2022**, *16*, 2100419.
[5] V. C. S. Theja, V. Karthikeyan, C. C. Yeung, S. Venkatesh, S. Nayak, V. A. L. Roy, *J. Alloys Compd.* **2022**, *900*, 163433.
[6] N. Nandihalli, C. J. Liu, T. Mori, *Nano Energy* **2020**, *78*, 105186.
[7] A. J. Minnich, M. S. Dresselhaus, Z. F. Ren, G. Chen, *Energy Environ. Sci.* **2009**, *2*, 466.
[8] Y. Lin, M. Wood, K. Imasato, J. J. Kuo, D. Lam, A. N. Mortazavi, T. J. Slade, S. A. Hodge, K. Xi, M. G. Kanatzidis, D. R. Clarke, M. C. Hersam, G. J. Snyder, *Energy Environ. Sci.* **2020**, *13*, 4114.
[9] C. Chen, Z. Zhang, J. Chen, *Front. Energy Res.* **2018**, *6*, 34.
[10] X. Du, P. Hu, T. Mao, Q. Song, P. Qiu, X. Shi, L. Chen, *ACS Appl. Mater. Interfaces* **2019**, *11*, 32151.
[11] D. Shiojiri, T. Iida, H. Kakio, M. Yamaguchi, N. Hirayama, Y. Imai, *J. Alloys Compd.* **2022**, *891*, 161968.
[12] Y. Mao, Y. Fang, K. Yuan, F. Huang, *J. Alloys Compd.* **2022**, *903*, 163921.
[13] V. Karthikeyan, S. L. Oo, J. U. Surjadi, X. Li, V. C. S. Theja, V. Kannan, S. C. Lau, Y. Lu, K. H. Lam, V. A. L. Roy, *ACS Appl. Mater. Interfaces* **2021**, *13*, 58701.
[14] J. Mao, Y. Wu, S. Song, Q. Zhu, J. Shuai, Z. Liu, Y. Pei, Z. Ren, *ACS Energy Lett.* **2017**, *2*, 2245.
[15] V. Karthikeyan, C. M. Arava, M. Z. Hlaing, B. Chen, C. H. Chan, K. H. Lam, V. A. L. Roy, *Scr. Mater.* **2020**, *174*, 95.
[16] R. Freer, A. V. Powell, *J. Mater. Chem. C* **2020**, *8*, 441.
[17] T. Tanishita, K. Suekuni, H. Nishiate, C. H. Lee, M. Ohtaki, *Phys. Chem. Chem. Phys.* **2020**, *22*, 2081.
[18] J. H. Pi, G. E. Lee, I. H. Kim, *J. Electron. Mater.* **2020**, *49*, 2755.
[19] Y. Goto, Y. Sakai, Y. Kamihara, M. Matoba, *J. Phys. Soc. Jpn.* **2015**, *84*, 044706.
[20] K. Chen, C. di Paola, B. Du, R. Zhang, S. Laricchia, N. Bonini, C. Weber, I. Abrahams, H. Yan, M. Reece, *J. Mater. Chem. C* **2018**, *6*, 8546.
[21] J. Yang, X.-L. Shi, Q. Yang, W. Shen, M. Li, Z. Zhang, W.-D. Liu, C. Fang, Y. Mao, Q. Wang, L. Chen, B. Wan, Y. Zhang, X. Jia, Z.-G. Chen, *Chem. Eng. J.* **2023**, *469*, 143965.
[22] G. E. Lee, J. H. Pi, I. H. Kim, *J. Electron. Mater.* **2020**, *49*, 2781.
[23] V. C. S. Theja, V. Karthikeyan, D. S. Assi, S. Gopalan, V. A. L. Roy, *ACS Omega* **2022**, *7*, 48484.
[24] J. Sun, D. Guo, H. Zhang, Z. Xu, C. Li, K. Li, B. Shao, D. Chen, Y. Ma, *J. Alloys Compd.* **2022**, *906*, 164299.
[25] V. C. S. Theja, V. Karthikeyan, D. S. Assi, V. A. L. Roy, *ACS Appl. Electron. Mater.* **2022**, *4*, 4781.
[26] L. L. Huang, J. Zhang, Z. M. Wang, X. G. Zhu, J. M. Li, C. Zhu, D. Li, C. J. Song, H. X. Xin, X. Y. Qin, *Materialia* **2018**, *3*, 169.
[27] S. Ghosh, S. M. Valiyaveettil, G. Shankar, T. Maity, K. H. Chen, K. Biswas, S. Suwas, R. C. Mallik, *ACS Appl. Energy Mater.* **2020**, *3*, 635.
[28] S. Ghosh, S. Tippireddy, G. Shankar, A. Karati, G. Rogl, P. Rogl, E. Bauer, S. R. K. Malladi, B. S. Murty, S. Suwas, R. C. Mallik, *J. Alloys Compd.* **2021**, *880*, 160532.
[29] W. J. Xie, J. He, S. Zhu, X. L. Su, S. Y. Wang, T. Holgate, J. W. Graff, V. Ponnambalam, S. J. Poon, X. F. Tang, Q. J. Zhang, T. M. Tritt, *Acta Mater.* **2010**, *58*, 4705.
[30] A. Ivanova, A. Novitskii, I. Serhiienko, G. Guélou, T. Sviridova, S. Novikov, M. Gorshenkov, A. Bogach, A. Korotitskiy, A. Voronin, A. Burkov, T. Mori, V. Khovaylo, *J. Mater. Chem. A* **2023**, *11*, 2334.

[31] J. Eilertsen, S. Rouvimov, M. A. Subramanian, *Acta Mater.* **2012**, *60*, 2178.
[32] W. J. Xie, Y. G. Yan, S. Zhu, M. Zhou, S. Populoh, K. Gałązka, S. J. Poon, A. Weidenkaff, J. He, X. F. Tang, T. M. Tritt, *Acta Mater.* **2013**, *61*, 2087.
[33] S. Zhu, W. Xie, D. Thompson, T. Holgate, M. Zhou, Y. Yan, T. M. Tritt, *J. Mater. Res.* **2011**, *26*, 1894.
[34] J. S. Dyck, B. Mao, J. Wang, S. Dorroh, C. Burda, *J. Electron. Mater.* **2012**, *41*, 1408.
[35] B. Madavali, H. S. Kim, K. H. Lee, S. J. Hong, *J. Appl. Phys.* **2017**, *121*, 225104.
[36] A. Ostovari Moghaddam, A. Shokuhfar, Y. Zhang, T. Zhang, D. Cadavid, J. Arbiol, A. Cabot, *Adv. Mater. Interfaces* **2019**, *6*, 1900467.
[37] A. K. Vivekanandan, C. W. Lee, R. Z. Wu, W. H. Tsai, S. H. Chen, Y. Y. Chen, C. T. Lin, *Nanomaterials* **2022**, *12*, 2032.
[38] C. Gayner, Y. Amouyal, *Adv. Funct. Mater.* **2020**, *30*, 1901789.
[39] H. S. Kim, Z. M. Gibbs, Y. Tang, H. Wang, G. J. Snyder, *APL Mater.* **2015**, *3*, 041506.
[40] X. L. Shi, K. Zheng, W. Di Liu, Y. Wang, Y. Z. Yang, Z. G. Chen, J. Zou, *Adv. Energy Mater.* **2018**, *8*, 1800775.
[41] B. Madavali, H. S. Kim, K. H. Lee, S. J. Hong, *Intermetallics* **2017**, *82*, 68.
[42] D. Chen, Y. Zhao, Y. Chen, T. Lu, Y. Wang, J. Zhou, Z. Liang, *Adv. Electron. Mater.* **2016**, *2*, 1500473.
[43] G. E. Lee, I. H. Kim, *J. Korean Inst. Met. Mater.* **2022**, *60*, 384.